Journal of Catalysis 286 (2012) 172–183

Contents lists available at SciVerse ScienceDirect

Journal of Catalysis

journal homepage: www.elsevier.com/locate/jcat

Enhanced selective nitroarene hydrogenation over Au supported on β-Mo_2C and β-Mo_2C/Al_2O_3

Noémie Perret [a], Xiaodong Wang [a], Laurent Delannoy [b], Claude Potvin [b], Catherine Louis [b], Mark A. Keane [a,*]

[a] Chemical Engineering, School of Engineering and Physical Sciences, Heriot-Watt University, Edinburgh EH14 4AS, Scotland, United Kingdom
[b] Laboratoire de Réactivité de Surface, UMR 7197 CNRS, Université Pierre et Marie Curie-Paris 06, 4 Place Jussieu, 75252 Paris Cedex 05, France

ARTICLE INFO

Article history:
Received 2 September 2011
Revised 24 October 2011
Accepted 27 October 2011
Available online 6 December 2011

Keywords:
Mo carbide
Supported Au
Selective hydrogenation
Chloronitrobenzene
Dinitrobenzene

ABSTRACT

β-Mo_2C and β-Mo_2C/Al_2O_3 have been synthesised *via* temperature programmed carburisation and employed, for the first time, as supports for gold catalysts. 1%w/w Au/Mo_2C and $Au/Mo_2C/Al_2O_3$ were prepared by deposition–precipitation with urea and used to promote the gas phase hydrogenation of *para*-chloronitrobenzene (*p*-CNB) and *meta*-dinitrobenzene (*m*-DNB) where 1% w/w Au/Al_2O_3 served as a reference catalyst. The supports and supported Au catalysts have been characterised in terms of point of zero charge, temperature programmed reduction (TPR), powder X-ray diffraction (XRD), X-ray photoelectron spectroscopy (XPS) and transmission electron microscopy (TEM) measurements. Both Mo_2C and Mo_2C/Al_2O_3 exhibited hydrogenation activity that was significantly enhanced with the incorporation of Au. XPS and elemental analysis of Mo_2C/Al_2O_3 revealed a lesser carbidic character and the presence of free surface carbon. Moreover, preparation of $Au/Mo_2C/Al_2O_3$ was accompanied by a leaching of the Mo component into solution. The carbide-based catalysts were characterised by a broader distribution of larger Au particles compared with the reference Au/Al_2O_3, which can be attributed to weaker Au/carbide interactions resulting in Au agglomeration during synthesis and activation. Nevertheless, the carbide systems delivered higher hydrogenation rates relative to Au/Al_2O_3. All the Au catalysts tested exhibited 100% selectivity to the target *p*-chloroaniline product in *p*-CNB hydrogenation. In the case of *m*-DNB, both nitro groups were hydrogenated to generate *m*-phenylenediamine as principal product for reaction over Au/Al_2O_3 whereas Au/Mo_2C promoted the exclusive production of *m*-nitroaniline at low conversions. The results demonstrate a synergistic effect between Au and Mo_2C that can be exploited in the cleaner production of commercially important aromatic amines.

1. Introduction

It is known that molybdenum carbide exhibits catalytic properties that are similar to noble metals (*e.g.* Pd and Ru) [1]. Indeed, carbides have been shown to be promising catalysts in ammonia synthesis [2], thiophene [3] and dibenzothiophene [4] hydrodesulfurisation, Fischer–Tropsch processing [5], the water gas shift reaction [6], alcohol steam reforming [7] and *n*-butane hydrogenolysis [8]. In comparison with noble metal catalysts, carbides are less expensive to produce and are tolerant to sulphur poisoning [7]. Moreover, in hydrogenation reactions [9], carbides exhibit selectivities that are quite distinct from Group VIII metal catalysts but this response has yet to be fully exploited. Molybdenum carbide can adopt a face-centred cubic (*fcc*, α-MoC_{1-x}), orthorhombic (α-Mo_2C) and hexagonal close packed (*hcp*, β-Mo_2C) crystal structure [9,10]. The particular crystalline phase, which is dependent on the method of synthesis, exhibits different catalytic behaviour [11]. Molybdenum carbides can be prepared by the reaction of graphite with vapourised Mo metal or MoO_3 but this method generates a low surface area material (1–2 $m^2\,g^{-1}$) and delivers a low product yield [12]. The principal means of Mo carbide synthesis involves temperature programmed nitridation and carburisation or direct carburisation [9]. A reduction and nitridation of MoO_3 (with NH_3) generates *fcc* Mo nitride that, in a subsequent carburisation step (in *e.g.* CH_4/H_2), can be converted to *fcc* α-MoC_{1-x} [5]. Alternatively, a direct carburisation of MoO_3 (to 900–1000 K) yields *hcp* β-Mo_2C [13]. Both approaches can produce a high surface area carbide (40–200 $m^2\,g^{-1}$) at high yield where the variables that impact on surface area include heating rate [14], gas space velocity [15], carbon source (*e.g.* CH_4, C_2H_6 and C_3H_8) [16,17] and % v/v H_2 in the feed [18]. It is also possible to deposit the Mo oxide precursor on a support (*e.g.* Al_2O_3), which with carburisation generates Mo_2C/Al_2O_3 [3,19]. The resultant dispersion on the carrier can result in enhanced catalytic performance relative to the bulk carbide

* Corresponding author.
E-mail address: M.A.Keane@hw.ac.uk (M.A. Keane).

0021-9517/$ - see front matter © 2011 Elsevier Inc. All rights reserved.
doi:10.1016/j.jcat.2011.10.026

[20,21]. Moreover, the incorporation of a transition metal (*e.g.* Ni [22] or Pt [7,23]) with Mo carbide has also been shown to influence catalytic activity [23] and selectivity [7]. In terms of hydrogenation, the focus of this study, Mo_2C has been used to promote the conversion of cyclohexene [24], naphthalene [21], benzene [20] and toluene [25]. However, a search through the literature did not unearth any reported study of the gas phase hydrogenation of aromatic nitro compounds over Mo carbide.

Gold catalysts deliver lower hydrogenation activity relative to conventional transition metal (Pd, Pt and Ni) catalysts as a result of a less effective activation/dissociation of H_2 [26]. In the hydrogenation of nitro compounds [27], ketones [28], aldehydes [29] and dienes [30], gold catalysts can exhibit enhanced selectivity to the target product. Activity and selectivity for hydrogenation reactions are dependent on Au particle size where significant catalytic activity requires a well dispersed Au phase (particles < 5 nm) [31]. Moreover, it has been shown that electron transfer from the support to nano-sized Au particles influences the catalytic response [32]. Of direct relevance to this study is the finding of Florez and coworkers [33] that charge transfer in Au-carbide systems is greater than that observed for oxide supports. In previous publications [32,34–36], we have demonstrated exclusivity (with respect to $-NO_2$ reduction) in the gas phase continuous hydrogenation of a range of polyfunctional nitroarenes over Au supported on Al_2O_3, TiO_2, Fe_2O_3 and CeO_2. The goal of this study is to combine the catalytic properties of Mo carbide and Au in order to achieve a synergy that elevates reaction rate while maintaining hydrogenation selectivity. *para*-Chloroaniline (*p*-CAN) and *meta*-nitroaniline (*m*-NAN) are commercially important chemicals in the manufacture of polymers, dyes and agrochemicals [37]. Conventional synthesis routes exhibit serious drawbacks in terms of low selectivity to the target amine with the generation of appreciable toxic waste [38]. We report here the first synthesis and use of Au/Mo_2C and $Au/Mo_2C/Al_2O_3$ to promote the hydrogenation of *para*-chloronitrobenzene (*p*-CNB) and *meta*-dinitrobenzene (*m*-DNB). We compare the catalytic response with that obtained using Au/Al_2O_3 as a benchmark and correlate the catalytic data with critical catalyst structural characteristics.

2. Experimental

2.1. Catalyst preparation and activation

Bulk β-Mo_2C was synthesised *via* the temperature programmed carburisation of ammonium heptamolybdate tetrahydrate ($(NH_4)_6Mo_7O_{24}{\cdot}4H_2O$, Merck (99%)) in 80 cm^3 min^{-1} 20% v/v CH_4 (99.995%, Air Liquide) in H_2 (99.995%, Air Liquide). The temperature was ramped at 1 K min^{-1} to 973 K, maintained for 1 h and cooled to room temperature under H_2 with sample passivation in 1% v/v O_2/Ar (30 cm^3 min^{-1}) for 1 h. The passivation step was necessary to circumvent autothermal oxidation upon contact with air [39]. In the preparation of δ-alumina (Degussa) supported β-Mo_2C with a nominal Mo_2C loading of 10% w/w, 5 g of support was mixed with 40 cm^3 solution containing 0.92 g $(NH_4)_6Mo_7O_{24}{\cdot}4H_2O$ and stirred for 1 h at room temperature. Water was removed on a rotary evaporator at 353 K under vacuum for *ca.* 1 h, and the solid was dried at 353 K for 12 h. The impregnated alumina was heated in 16 cm^3 min^{-1} Ar at 0.5 K min^{-1} and held at 673 K for 3 h. The sample was then contacted with 80 cm^3 min^{-1} 20% v/v CH_4/H_2 with temperature ramping from 673 to 873 K (1 K min^{-1}) and from 873 to 973 K (0.5 K min^{-1}); the final temperature was maintained for 1 h. The CH_4/H_2 flow was switched to H_2, and the sample was cooled to room temperature and passivated as above. The $(NH_4)_6Mo_7O_{24}{\cdot}4H_2O$ impregnated alumina was also calcined in air at 673 K for 4 h to obtain MoO_3/Al_2O_3, which was subjected to XPS analysis for comparison purposes with the carburised sample. Mo_2C and Mo_2C/Al_2O_3 supported Au (nominal loading = 1% w/w Au) were prepared by deposition–precipitation with urea [40], where 78 cm^3 distilled water and 2 cm^3 $HAuCl_4$ solution (10 g dm^{-3}) were introduced into a double-walled glass reactor, with water circulation at 353 K that facilitated accurate temperature control with vigorous stirring. A suspension of 1 g Mo_2C (or Mo_2C/Al_2O_3) in 20 cm^3 distilled water was immersed in an ultrasound bath for 2 min to enhance dispersion, and this was introduced to the glass reactor with the immediate addition of 400 mg solid urea. The suspension was stirred at 353 K for 16 h in the absence of light, the solution pH was monitored continuously, and the solid was separated by centrifugation and washed with 100 cm^3 distilled water. Washing was repeated four times, and the solid was dried under vacuum in a desiccator in the dark for *ca.* 12 h. For comparison purposes, a 1% w/w Au/δ-Al_2O_3 was also prepared using the procedure described above. The catalyst precursors (*as prepared* samples) were sieved into a batch of 75 μm average particle diameter and stored at 277 K under He in the dark.

2.2. Catalyst characterisation

The Au, Mo, Cl and Al contents of the *as prepared* samples were measured by inductively coupled plasma atom emission spectroscopy (CNRS Centre of Chemical Analysis, Vernaison). Carbon content was determined using an Exeter CE-440 Elemental Analyser after sample combustion at *ca.* 1873 K. The pH values associated with the point of zero charge (pH_{PZC}) of the supports were determined using the potentiometric mass titration technique [41]. For each support, three different masses (0.025, 0.050 and 0.075 g) were immersed in 50 cm^3 0.1 M NaCl to which a known amount of NaOH (0.1 M) had been added to adjust the pH to *ca.* 11. After stabilisation of the pH (*ca.* 1 h), titration of the samples was performed under continuous agitation in a He atmosphere with HCl (0.1 M) as titrant. The pH was measured using a pH meter (Hanna Instruments) equipped with a crystal-body electrode coupled to a data logging and collection system (Pico Technology Ltd.); calibration was performed with standard buffer solutions.

Temperature programmed reduction (TPR) and BET surface area were determined using the commercial CHEM-BET 3000 (Quantachrome) unit. Samples of Mo_2C, Al_2O_3, Mo_2C/Al_2O_3, Au/Mo_2C, $Au/Mo_2C/Al_2O_3$ and Au/Al_2O_3 were loaded into a U-shaped quartz cell (10 cm × 3.76 mm *i.d.*) and heated in 16 cm^3 min^{-1} (Brooks mass flow controlled) 5% v/v H_2/N_2 at 2 K min^{-1} to 573 ± 1 K. The effluent gas passed through a liquid N_2 trap and changes in H_2 consumption were monitored by TCD with data acquisition/manipulation using the TPR Win™ software. The activated samples were maintained at the final temperature in a constant flow of H_2/N_2 for 4 h, swept with 65 cm^3 min^{-1} N_2 for 1.5 h and cooled to room temperature. The passivation treatment of the carbides can be taken to result in a monolayer oxygen coverage. The H_2 consumption (mmol $g_{Mo_2C}^{-1}$) during TPR then represents the amount required to remove this passivating monolayer

$$O\ (s) + 3/2H_2\ (g) \rightarrow H\ (s) + H_2O\ (g) \quad (1)$$

where (s) indicates surface atoms and (g) the gas phase. Taking a stoichiometry of two oxygen atoms per Mo atom [42], the β-Mo_2C surface area (SA_{TPR}, $m^2 g_{Mo_2C}^{-1}$) can be calculated from

$$SA_{TPR}\left(m^2\ g_{Mo_2C}^{-1}\right) = (2/3) \times n_{H_2} \times N_A/(2 \times N_{Mo}) \quad (2)$$

where n_{H_2} represents moles of H_2 consumed during TPR per gram Mo_2C (H_2 consumption, Table 1) and N_A is the Avogadro number. On the assumption that the surface of Mo_2C consists of an equal proportion of the main low index planes, an approximate Mo

Table 1
Au and Mo_2C content (% w/w), Mo/C ratio, BET surface area (SA_{BET}), H_2 consumption during TPR and specific Mo_2C surface area calculated from TPR measurements (SA_{TPR}), Au particle size range, surface area weighted mean Au diameter (d_{TEM}) and dispersion (D).

Catalyst	Au (% w/w)	Mo_2C (% w/w)	Mo/C	SA_{BET} ($m^2\ g^{-1}$)	H_2 consumption (mmol $g_{Mo_2C^{-1}}$)	SA_{TPR} ($m^2 g_{Mo_2C^{-1}}$)	Au size range[a]/d_{TEM} (nm)	D
Mo_2C	–	100	1.8	39	1.6	34	–	–
Mo_2C/Al_2O_3	–	12.1	1.5	82	5.2	110	–	–
Au/Mo_2C	0.94	99.1	1.7	47	1.7	36	4–20/13.4	0.09
$Au/Mo_2C/Al_2O_3$	1.03	5.6	1.5	89	5.5	116	6–12/8.3	0.15
Au/Al_2O_3	0.95	–	–	91	0.1[b]	–	1–3/2.3	0.54

[a] From TEM analysis.
[b] mmol H_2 consumed g^{-1} during TPR.

surface density (N_{Mo}) is given by 1×10^{19} Mo m^{-2} [42]. The BET surface area (SA_{BET}) was determined (after TPR) in 30% v/v N_2/He using pure N_2 (99.9%) as internal standard. At least three cycles of N_2 adsorption–desorption in the flow mode were employed to determine total surface area by the standard single point method; areas were reproducible to within ±3%, and the values quoted in this paper represent the mean. Post-BET area measurement, the samples were passivated (as described above) for off-line analysis.

Powder X-ray diffractograms were recorded on a Bruker/Siemens D500 incident X-ray diffractometer using Cu Kα radiation. The samples were scanned at a rate of 0.02° $step^{-1}$ over the range $5° \leq 2\theta \leq 80°$. Diffractograms were identified using the JCPDS-ICDD reference standards, *i.e.*, β-Mo_2C (Card No. 11-0680), δ-Al_2O_3 (16-394) and Au (04-784). The Au metal particle size (d_{hkl}) was estimated using the Scherrer equation

$$d_{hkl} = \frac{K \times \lambda}{\beta \times \cos\theta} \tag{3}$$

where $K = 0.9$, λ is the incident radiation wavelength (1.5056 Å), β is the peak width at half the maximum intensity, and θ represents the diffraction angle corresponding to the (2 0 0) plane associated with metallic Au ($2\theta = 44.5°$). Transmission electron microscopy (TEM) combined with Energy-Dispersive X-ray spectroscopy (EDX) analysis was performed using a JEOL 2010 electron microscope operating at 200 kV. Samples for analysis were crushed and homogenously dispersed in ethanol by ultrasonication, and a drop of the suspension was deposited on a carbon-coated copper grid and evaporated. The surface area weighted Au particle diameter was calculated from

$$d_{TEM} = \frac{\sum_i n_i d_i^3}{\sum_i n_i d_i^2} \tag{4}$$

where n_i is the number of particles of diameter d_i. XPS spectra were collected on a SPECS (Phoibos MCD 150) X-ray photoelectron spectrometer, using a Mg Kα ($h\nu$ = 1253.6 eV) X-ray source. The samples were reduced by TPR and passivated before transfer in air to the XPS chamber. After collection, the binding energies were calibrated with respect to the C—C/C—H components of the C *1s* peak (binding energy = 284.6 eV). All spectra processing was carried out using the Casa XPS software package.

2.3. Catalysis procedure

Reactions were conducted under atmospheric pressure at 423–473 K in a fixed bed vertical glass reactor (l = 450 mm; *i.d.* = 15 mm). The samples were activated (*in situ*) in 60 cm^3 min^{-1} H_2 at 2 K min^{-1} to 573 K, maintaining the final temperature for 1 h. The catalytic reactor and operating conditions to ensure negligible heat/mass transport limitations have been fully described elsewhere [43] but some features, pertinent to this study, are given below. A layer of borosilicate glass beads served as preheating zone, ensuring that the organic reactants were vapourised and reached reaction temperature before contacting the catalyst. Isothermal conditions (±1 K) were ensured by diluting the catalyst bed with ground glass (75 μm); the glass was mixed thoroughly with catalyst before insertion in the reactor. The reaction temperature was continuously monitored using a thermocouple inserted in a thermowell within the catalyst bed. The reactants, *p*-CNB and *m*-DNB, as solutions in ethanol, were delivered at a fixed calibrated flow rate to the reactor *via* a glass/Teflon air-tight syringe and Teflon line using a microprocessor controlled infusion pump (Model 100 kd Scientific). A co-current flow of *p*-CNB (or *m*-DNB) and ultrapure (>99.99%, BOC) H_2 (<1% v/v organic in H_2) was maintained at a $GHSV = 2 \times 10^4\ h^{-1}$ with an inlet reactant molar flow (F) in the range $4–39 \times 10^{-5}$ $mol_{p\text{-CNB}}\ h^{-1}$ (or $2–10 \times 10^{-5}$ $mol_{m\text{-DNB}}\ h^{-1}$). The H_2 content in the feed was up to 2400 times in excess of the stoichiometric requirement. Hydrogen flow rate was monitored using a Humonics (Model 520) digital flowmeter. The ratio of mass of catalyst to inlet molar organic feed rate (m/F) spanned the range 76—1250 g h $mol_{p\text{-CNB}}^{-1}$ (or 3—2500 g h $mol_{m\text{-DNB}}^{-1}$). In a series of blank tests, passage of both reactants in a stream of H_2 through the empty reactor or over the Al_2O_3 support did not result in any detectable conversion. The reactor effluent was frozen in a liquid nitrogen trap for subsequent analysis, which was made using a Perkin-Elmer Auto System XL gas chromatograph equipped with a programmed split/splitless injector and a flame ionisation detector, employing a DB-1 (50 m × 0.33 mm, 0.20 μm film thickness) capillary column (J&W Scientific). *p*-CNB (Sigma–Aldrich, purity ⩾99%), *m*-DNB (Fluka, ⩾98%) and ethanol (Sigma Aldrich, ⩾99%) were used as supplied without further purification. Taking the hydrogenation of *p*-CNB as representative, activity is quantified in terms of fractional conversion ($x_{p\text{-CNB}}$)

$$x_{p\text{-CNB}} = \frac{[p\text{-CNB}]_{in} - [p\text{-CNB}]_{out}}{[p\text{-CNB}]_{in}} \tag{5}$$

where selectivity with respect to *p*-chloroaniline (*p*-CAN) is given by

$$S_{p\text{-CAN}}\% = \frac{[p\text{-CAN}]_{out}}{[p\text{-CNB}]_{in} - [p\text{-CNB}]_{out}} \times 100 \tag{6}$$

and [*p*-CNB] and [*p*-CAN] are, respectively, the concentrations of *p*-CNB and *p*-CAN; the subscripts *in* and *out* refer to the inlet and outlet streams. Repeated reactions with samples from the same batch of catalyst delivered conversion/selectivity values that were reproducible to within ±3%.

3. Result and discussion

3.1. Catalyst characterisation

Elemental analysis (see Table 1) indicates that the deposition–precipitation procedure was efficient in preparing Au loaded on Al_2O_3, Mo_2C and Mo_2C/Al_2O_3 with a gold content of *ca.* 1% w/w. The pH associated with the point of zero charge (pH_{PZC}) is a critical

property of the support that determines the solution pH requirements to ensure precursor-support interactions during catalyst preparation by deposition–precipitation [40,44,45]. The associated titration curves for the supports (Fig. 1) show that the pH_{PZC} for Mo_2C (2.9) and Mo_2C/Al_2O_3 (3.7) is much lower than that measured for Al_2O_3 (7.5). The gold loadings achieved in this study are significant given that the pH_{PZC} values for Mo_2C and Mo_2C/Al_2O_3 are lower than *ca.* 5, the pH which has been identified as a prerequisite for effective deposition of the gold precursor on metal oxide and carbon supports [45]. When the solution pH < pH_{PZC}, the support surface bears a positive charge (due to protonation), favouring interaction with anionic species in solution and a pH in excess of pH_{PZC} results in a surface affinity for cationic species [46]. It is known that, in aqueous solution, $AuCl_4^-$ undergoes a sequential substitution of Cl^- with OH^- at pH = 4, 4.6, 6.5 and 9, at which point $Au(OH)_4^-$ predominates [45,47]. The temporal pH variations in the preparation of Au/Mo_2C, Au/Al_2O_3 and $Au/Mo_2C/Al_2O_3$ are given in Fig. 2 where the pH_{PZC} of each support is identified as a dashed line. The observed temporal increase in pH corresponds to a progressive neutralisation of the acidity of the $HAuCl_4$ solution by OH^- generated *via* the decomposition of urea. In the case of Al_2O_3 (Fig. 2b), the initial solution pH (3.1) was far below the pH_{PZC} and the subsequent pH increase ultimately converged with the pH_{PZC}. Under these synthesis conditions, pH < pH_{PZC} over the first 2–3 h of deposition–precipitation and Au precursor interactions with the (positively) charged Al_2O_3 were facilitated. However, solution pH in the preparation of Au/Mo_2C (Fig. 2a) and $Au/Mo_2C/Al_2O_3$ (Fig. 2c) exceeded the associated support pH_{PZC}. As a

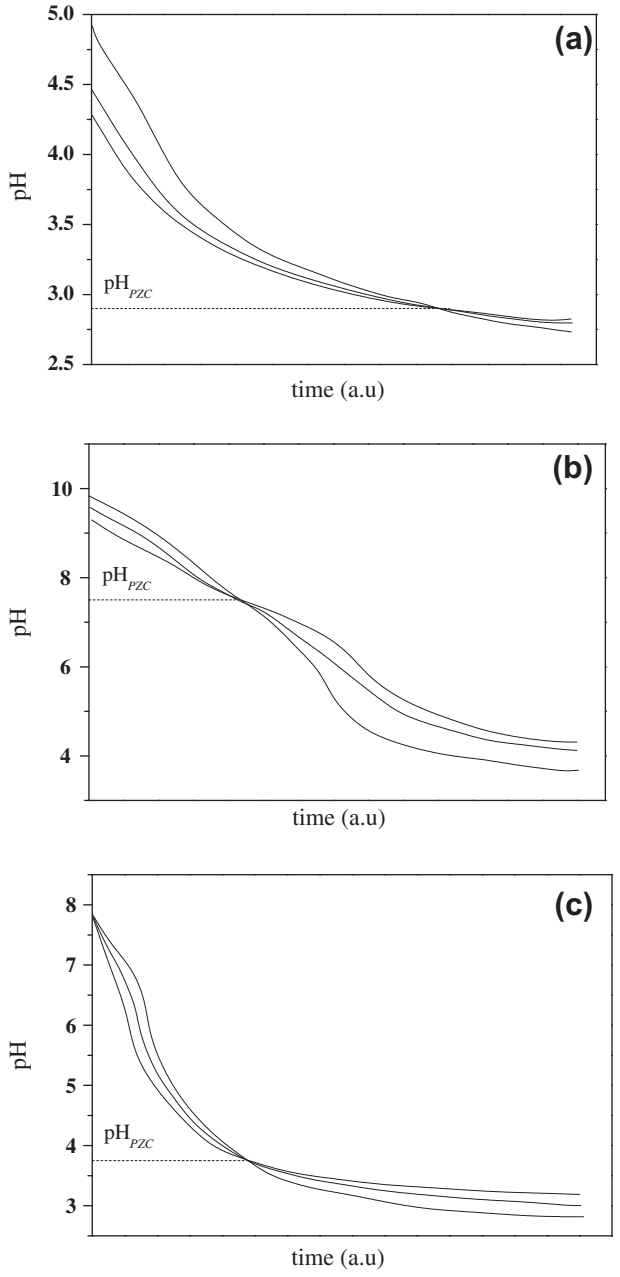

Fig. 1. pH profiles associated with the pH of point of zero charge (pH_{PZC}) measurement for (a) Mo_2C, (b) Al_2O_3 and (c) Mo_2C/Al_2O_3.

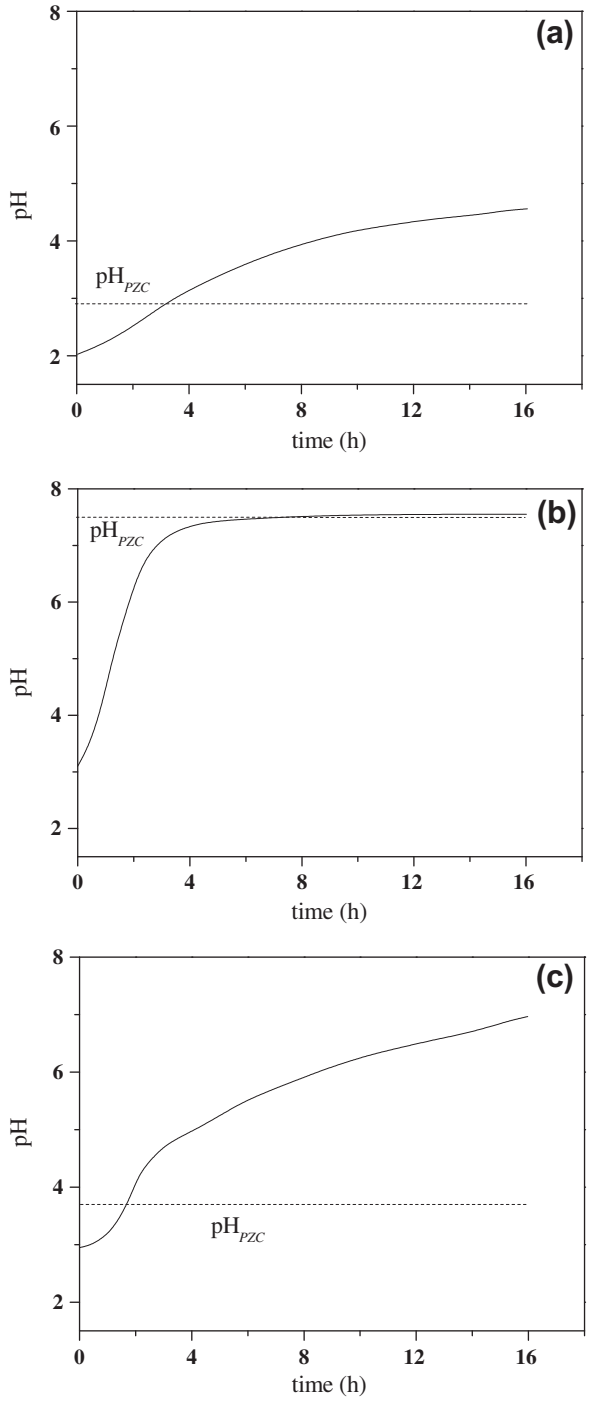

Fig. 2. Temporal pH variations in the preparation of (a) Au/Mo_2C, (b) Au/Al_2O_3 and (c) $Au/Mo_2C/Al_2O_3$. Note: dashed lines identify pH_{PZC} of the supports.

consequence, interactions of anionic Au precursor species with the negatively charged support were not favoured and deposition occurred principally *via* physical (as opposed to electrostatic) adsorption effects.

XRD patterns of Mo_2C (I), Au/Mo_2C (II), Al_2O_3 (III), Au/Al_2O_3 (IV), Mo_2C/Al_2O_3 (V) and $Au/Mo_2C/Al_2O_3$ (VI) are presented in Fig. 3. The XRD profile (I) of Mo_2C presents peaks that are characteristics of hexagonal β-Mo_2C. There was no evidence of any bulk oxide (MoO_3 or MoO_2) present in the carburised sample, *i.e.* the oxide precursor had been completely converted to the carbide and the passivation procedure resulted in a superficial (as opposed to bulk) oxidation. The TPR profile for Mo_2C is presented in Fig. 4I, and the H_2 consumption required to remove the passivation layer is given in Table 1. The TPR profile is characterised by a maximum H_2 consumption at 493 K with a lower temperature shoulder to the main peak. The amount of H_2 consumed was used to calculate the specific Mo_2C surface area (SA_{TPR}, see Eq. (2)), and the result (34 $m^2\ g^{-1}$) is in good agreement with the value obtained by standard BET analysis (39 $m^2\ g^{-1}$). The introduction of Au resulted in a shift in the reduction temperature to a lower value (by *ca.* 40 K, see Fig. 4II) for Au/Mo_2C. A similar effect has been noted for Au supported on reducible carriers, *e.g.*, Fe_2O_3 [48] and CeO_2 [30], with a decrease in the temperature required for a partial reduction of the support (by up to 400 K). The XRD pattern for Au/Mo_2C *post-activation* (Fig. 3II) exhibits the principal planes for β-Mo_2C with evidence of a signal due to the (1 1 1) plane of metallic Au

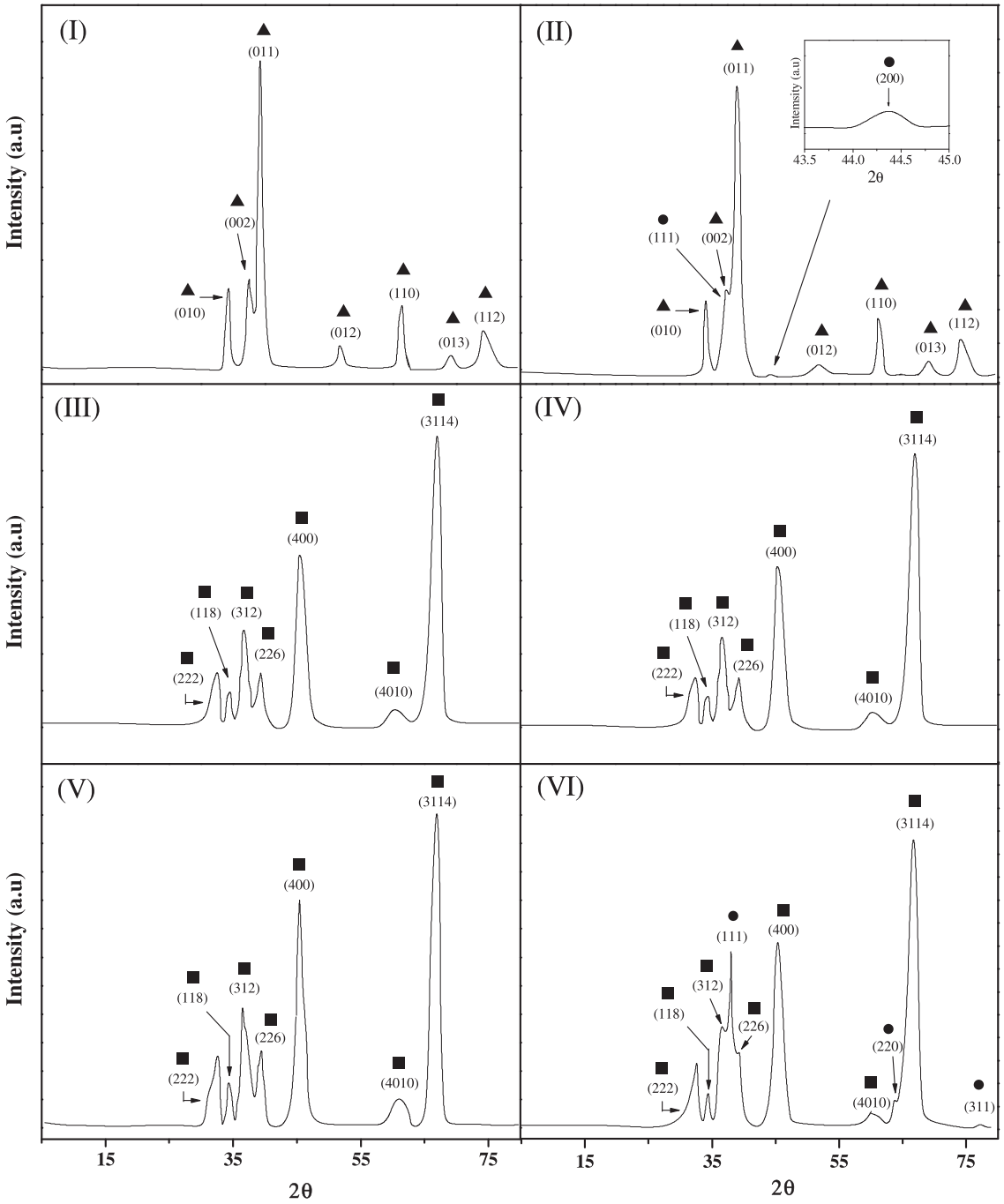

Fig. 3. XRD patterns for Mo_2C (I), Au/Mo_2C (II), Al_2O_3 (III), Au/Al_2O_3 (IV), Mo_2C/Al_2O_3 (V) and $Au/Mo_2C/Al_2O_3$ (VI). Note: XRD peak assignments are based on JCPDS-ICDD reference standards: (▲) β-Mo_2C (Card No. 11-0680); (■) δ-Al_2O_3 (16-394); (●) Au (04-784).

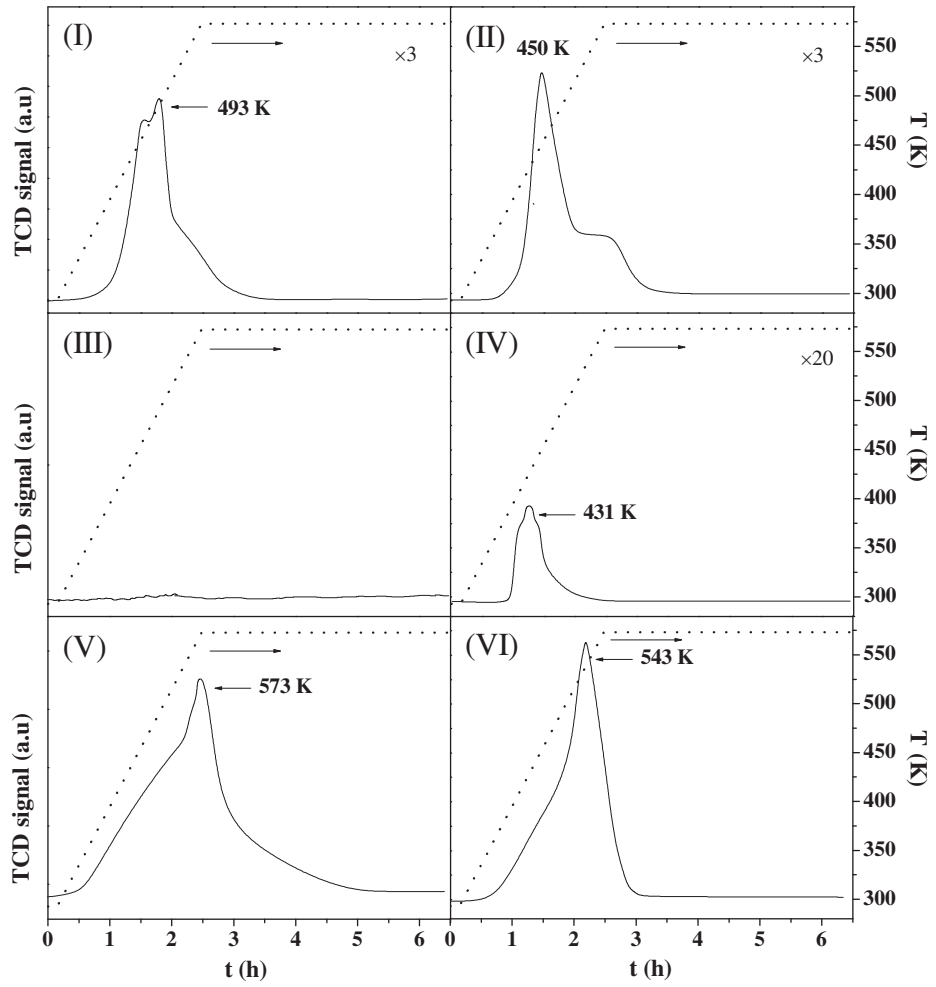

Fig. 4. TPR profiles for Mo_2C (I), Au/Mo_2C (II), Al_2O_3 (III), Au/Al_2O_3 (IV), Mo_2C/Al_2O_3 (V) and Au/Mo_2C/Al_2O_3 (VI).

($2\theta = 38.1°$) that overlaps with the (0 0 2) peak for the support ($2\theta = 37.9°$). A peak at 44.4° related to Au (2 0 0) is also detectable as shown in the inset to Fig. 3II. XRD analysis (pattern not shown) of the *as prepared* Au/Mo_2C also exhibited signals due to metallic Au, indicating that the gold precursor was reduced during preparation. The formation of metallic Au during catalyst synthesis has already been reported elsewhere, notably in the preparation of iron oxide supported Au by co-precipitation [49]. It should be noted that synthesis conditions were chosen in this study to avoid gold reduction, *i.e.,* preparation and storage in the dark with room temperature drying in an inert atmosphere. The standard redox potential of ionic Mo (*e.g.* E^0 for $H_2Mo^{VI}O_4/Mo^{IV}O_2 = +0.646$ V) is significantly lower than that for ionic Au (E^0 for $Au^{III}(OH)_3/Au^0 = +1.32$ V, E^0 for $Au^{III}Cl_4^-/Au^0 = +1.002$V) [50]. Surface oxidised Mo species (post-passivation), with a lower electrochemical potential, can act to reduce the Au precursor, resulting in a reductive deposition of Au. TEM–EDX analysis revealed a degree of heterogeneity associated with Au/Mo_2C and an apparent bimodal distribution of large (*ca.* 20 nm, Fig. 5A-1) and small (4–6 nm, Fig. 5A-2) Au particles; a representative EDX spectrum is included with image (A-2). A Cl content >300 ppm has been shown to induce the formation of large Au particles (>20 nm) [51] and poison catalyst activity [52]. However, in this study, the Cl content of all the catalysts was below detection limits (<200 ppm); *i.e.,* sample washing (see Section 2) was effective in removing residual Cl. The mean Au diameter obtained from TEM analysis (13.4 nm, see Table 1) is in good agreement with the value (16 nm) from XRD peak line broadening analysis, *i.e.,* application of Eq. (3). EDX surface mapping revealed areas of the Mo_2C support with a low (Au/Mo = 0.0012 in Fig. 5A-1) or undetectable Au content. The formation of larger gold particles has also been observed for Au on oxide carriers characterised by low pH_{PZC}, notably SiO_2, which delivered poor Au dispersion after deposition–precipitation with urea [40], as a direct consequence of weaker interaction with the support.

The TPR profile of δ-Al_2O_3 is featureless with no evidence of H_2 uptake (Fig. 4III), which was expected and is in agreement with the literature [53]. The TPR response exhibited by *as prepared* Au/Al_2O_3 is presented in Fig. 4IV and shows a single peak at 431 K. Hydrogen consumption during TPR matched that required for the reduction of the precursor to the metallic form, *i.e.,* $Au^{3+} \rightarrow Au^0$. An equivalent response in terms of Au reduction has been reported elsewhere with T_{max} at 434 K [35] and 436 K [54]. The BET surface area of Au/Al_2O_3 (91 $m^2\,g^{-1}$, Table 1) was lower than that of the starting Al_2O_3 support (101 $m^2\,g^{-1}$), which can be attributed to a partial pore filling by the metal component [55]. The XRD profiles for δ-Al_2O_3 (Fig. 3III) and Au/Al_2O_3 (Fig. 3IV) exhibit the seven main characteristic XRD peaks for δ-Al_2O_3. There was no observable XRD response due to Au, indicative of the formation of a well dispersed metallic phase. Indeed, Au particles with an average size of 2.3 nm were detected by TEM (Table 1), which is consistent with stronger metal/support interactions that limit particle agglomeration. This response finds agreement with previous reports of Au/Al_2O_3 prepared by deposition–precipitation with urea [40]. Representative low (B-1) and higher (B-2) magnification TEM

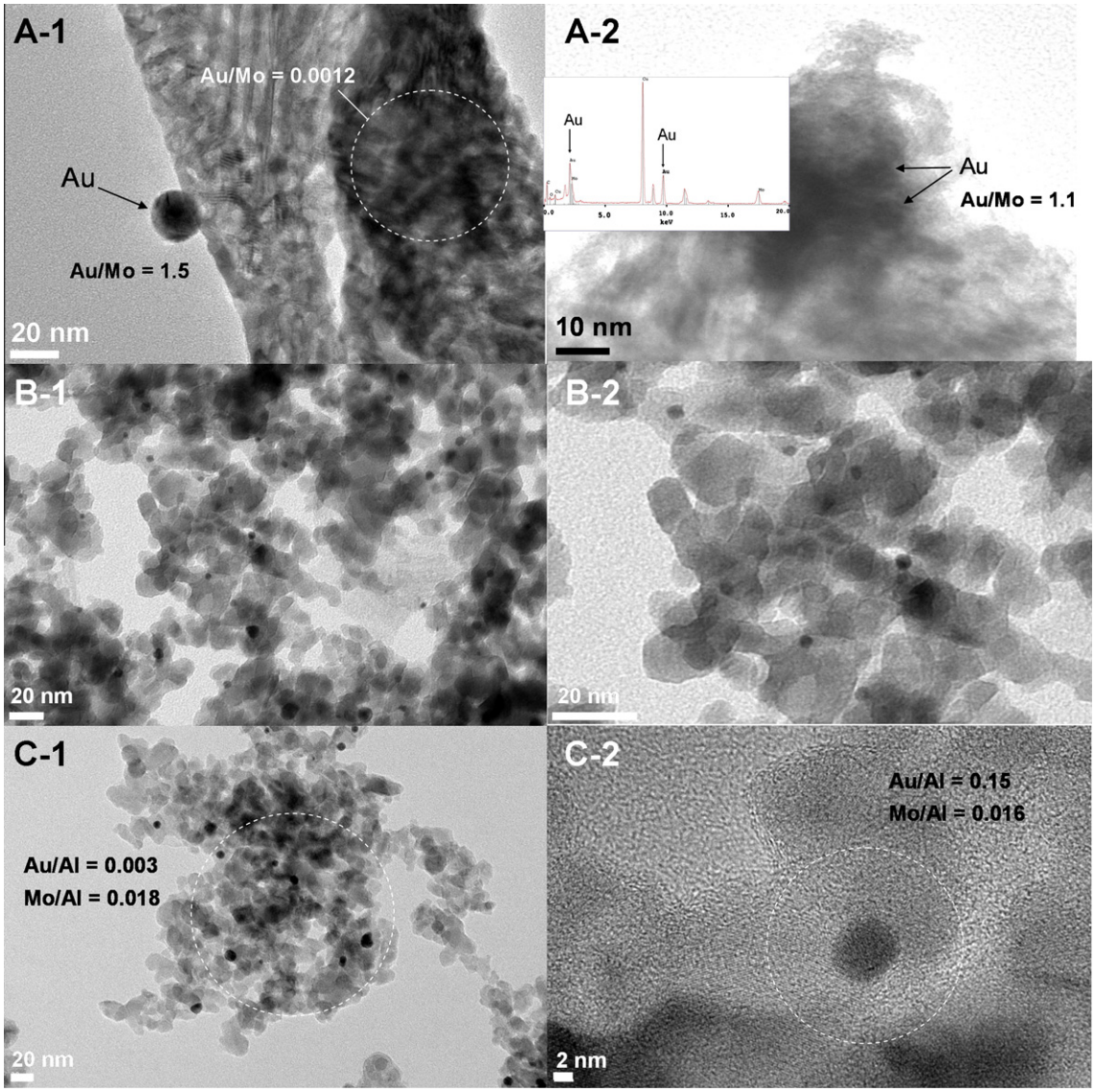

Fig. 5. Representative TEM images with EDX measurements over selected areas for Au/Mo_2C (A, with representative EDX spectrum in A-2), Au/Al_2O_3 (B) and $Au/Mo_2C/Al_2O_3$ (C).

images are presented in Fig. 5, where well dispersed pseudo-spherical particles (in the 1–3 nm range) are in evidence.

With regard to $Au/Mo_2C/Al_2O_3$, the Mo_2C loading was decreased by over a factor of 2 after Au deposition on the parent Mo_2C/Al_2O_3 (see Table 1). This loss of supported Mo_2C into solution can be attributed to a leaching of surface oxidised Mo, formed during the passivation step, into solution as H_2MoO_4 [56]. There were no detectable peaks due to Mo_2C in the XRD of Mo_2C/Al_2O_3 (Fig. 3(V)), which can be attributed to strong interaction between MoO_3 and Al_2O_3, resulting in finely dispersed Mo_2C [57]. Moreover, the four principal Mo_2C XRD peaks (at $\theta = 34.4°$, 37.9°, 39.4° and 61.6° associated with the (0 1 0), (0 0 2), (0 1 1) and (1 1 0) planes) overlap with the characteristic peaks (at $\theta = 34.5°$, 36.5°, 39.5° and 61.1°) for δ-Al_2O_3. It should be noted that the formation of Mo_2C supported on γ-Al_2O_3 has been reported previously using the same approach, *i.e.,* impregnation with $(NH_4)_6Mo_7O_{24}{\cdot}4H_2O$ and subsequent temperature programmed carburisation [3,58]. Carbon contents were measured, and the resultant Mo/C ratios (<2, see Table 1) suggest full carburisation of all the samples, where the occurrence of excess C can be due to the presence of free surface carbon [42]. The temperature requirement for surface reduction, *i.e.,* to remove the passivated layer, was significantly higher (by 80 K) for the alumina supported Mo_2C (Fig. 4V) relative to bulk Mo_2C (Fig. 4I). This has been noted elsewhere and attributed to interaction between the carbide and the alumina carrier [20,56]. Hydrogen consumption (per gram Mo_2C) during TPR was appreciably greater for Mo_2C/Al_2O_3 (5.2 mmol $g_{Mo_2C^{-1}}$, Table 1) relative to Mo_2C (1.6 mmol $g_{Mo_2C^{-1}}$), suggesting a dispersion effect. Indeed, the specific carbide surface area (SA_{TPR}) showed a significant increase on the alumina support, which was unaffected by the incorporation of Au. An invariance in surface area after Au deposition is consistent with the BET measurements (Table 1). As in the case of Au/Mo_2C, the presence of Au on Mo_2C/Al_2O_3 resulted in a shift in the TPR profile to a lower temperature (see Fig. 4VI). The XRD pattern (Fig. 3VI) for $Au/Mo_2C/Al_2O_3$ shows three peaks at 38.1°, 64.5° and 77.5°, which are characteristics of Au metal. TEM–EDX has demonstrated the presence of Au particles in the 6–12 nm size range with a mean particle size of 8.3 nm (Table 1), which is in good agreement with the Au particle size based on XRD line broadening (9 nm). A representative low magnification TEM image is presented in Fig. 5C-1 where EDX analysis of a large sample area (see dotted line circle) reveals the presence of both Au

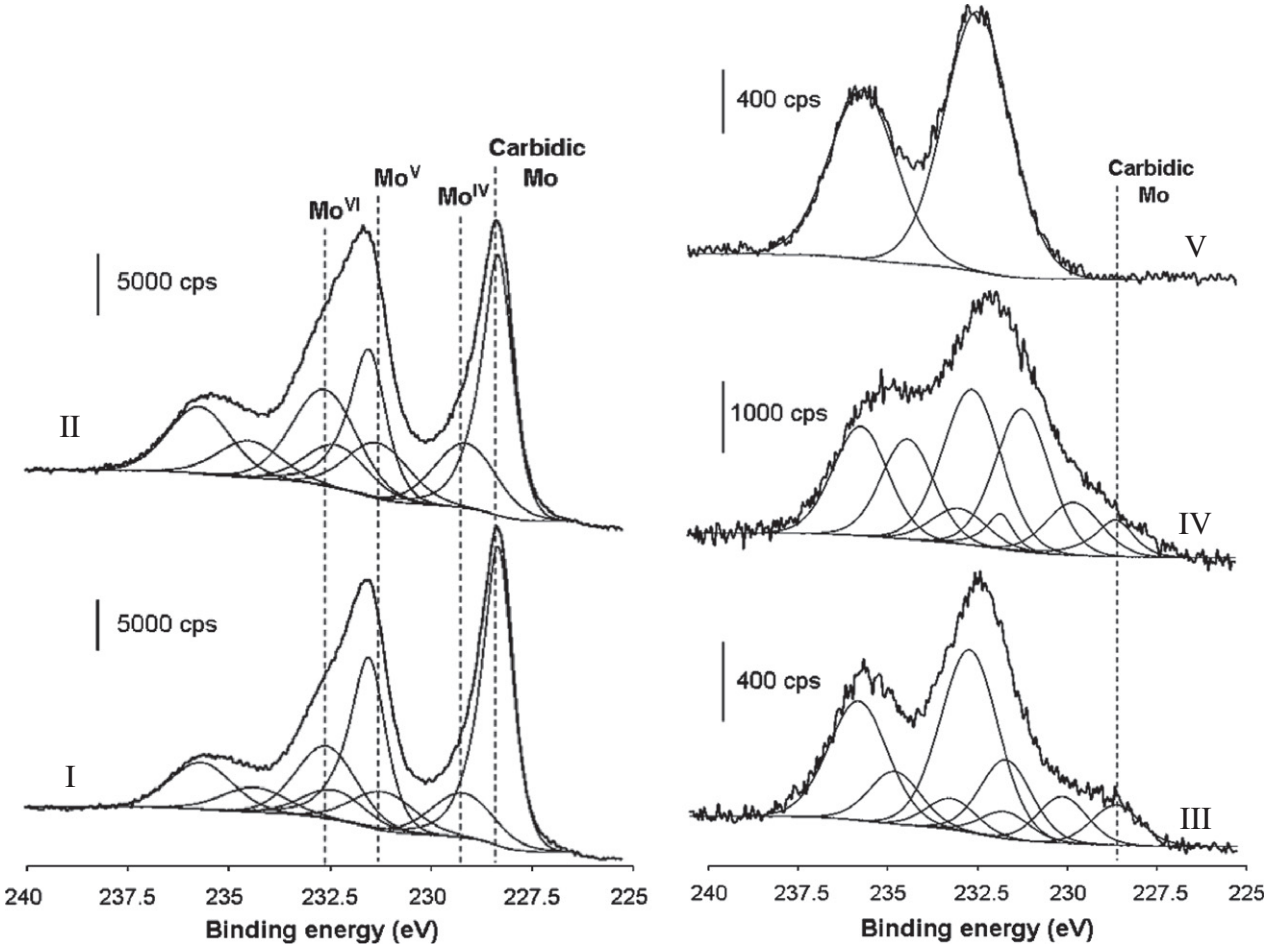

Fig. 6. XPS spectra over the Mo 3*d* region for Mo_2C (I), Au/Mo_2C (II), Mo_2C/Al_2O_3 (III), $Au/Mo_2C/Al_2O_3$ (IV) and MoO_3/Al_2O_3 (V).

and Mo with Au/Mo ratio (0.16) close to the nominal value (0.1) in terms of bulk content. Further EDX mapping (not shown) of areas with Mo/Al in the range = 0.015–0.019) showed no detectable Au.

XPS spectra over the Mo 3*d*, C *1s* and Au 4*f* binding energy (BE) regions are presented in Figs. 6 and 7. The Mo 3*d* profiles for Mo_2C (Fig. 6I) and Au/Mo_2C (Fig. 6II) are very similar and present, after deconvolution, a principal Mo $3d_{5/2}$ contribution at BE = 228.3 ± 0.2 eV, corresponding to carbidic Mo [24]. Signals at higher BE (and lower intensity) can be related to the presence of Mo in an oxidised state due to passivation, *i.e.,* Mo(IV) (229.2 ± 0.2 eV) [7], Mo(V) (231.2 ± 0.2 eV) [59] and Mo(VI) (232.5 ± 0.2 eV) [60]. The presence of higher oxidation state Mo species is also consistent with our proposed Mo promoted oxido-reduction of the anionic Au precursor during deposition–precipitation. The Mo 3*d* profile for Mo_2C/Al_2O_3 (Fig. 6III) coincides with that recorded for $Au/Mo_2C/Al_2O_3$ (Fig. 6IV), where a carbidic Mo contribution is visible although the molybdenum phase is predominantly in the form of Mo oxides, *i.e.,* Mo(IV), Mo(V) and Mo(VI), respectively, at BE = 229.4, 231.3 and 232.7 eV. Comparison with the spectrum generated for the calcined supported precursor (MoO_3/Al_2O_3, Fig. 6V) demonstrates that the carburisation procedure led to the formation of low oxidation state molybdenum species, *i.e.* carbidic Mo, Mo(IV) and Mo(V). Moreover, the presence of Mo_2C can be attested by the deconvoluted C *1s* spectra shown in Fig. 7I–IV, where a contribution due to carbidic carbon, at BE = 283.4 eV [61], is observed for all the catalysts. In addition, contributions assigned to graphitic carbon (BE = 284.6 eV) [62], C—O (BE = 286.3 eV) [7] and C═O (BE = 288.6 eV) [22] are also evident. XPS analysis of Mo_2C supported on zeolites [21] and Al_2O_3 [19,22] has generated similar spectra. Our XPS results reveal carbidic character for the alumina supported Mo_2C, *pre-* and *post*-Au incorporation that may be more consistent with a supported oxycarbide phase. Indeed, we should flag an IR-study by Wu et al. [63] that established the presence of $Mo^{\delta+}$ ($0 < \delta < 2$) in as prepared Mo_2C/Al_2O_3 where subsequent passivation resulted in superficial oxycarbide formation ($2 \leqslant \delta < 4$) with carbide regeneration by reduction in H_2. The Au $4f_{7/2}$ (BE = 84.0 ± 0.2 eV) and Au $4f_{5/2}$ (BE = 87.6 ± 0.2 eV) peaks for Au/Mo_2C (Fig. 7V) are characteristics of Au in the metallic state [64]. The Au $4f_{7/2}$ peaks for Au/Al_2O_3 (Fig. 7VII) and $Au/Mo_2C/Al_2O_3$ (Fig. 7VI) are both centred at 83.5 ± 0.2 eV. Similar values have been reported in the literature for Au/Al_2O_3 [65] and attributed to electron transfer from the support. The equivalence of the Au BE values in this study suggests that there is no detectable specific interaction between Au and Mo in $Au/Mo_2C/Al_2O_3$.

3.2. Catalytic activity/selectivity

Reaction selectivity is critical in *para*-chloronitrobenzene (*p*-CNB) and *meta*-dinitrobenzene (*m*-DNB) hydrogenation where a number of intermediates and by-products are possible, as identified in Fig. 8. We have shown in previous studies that the gas phase hydrogenation of *p*-CNB over Pd/Al_2O_3 generated nitrobenzene (hydrodechlorination) and aniline (hydrodechlorination/hydrogenation) as products [34] whereas supported Au exclusively produced *p*-chloroaniline (*p*-CAN) [32,34,35]. The hydrogenation of

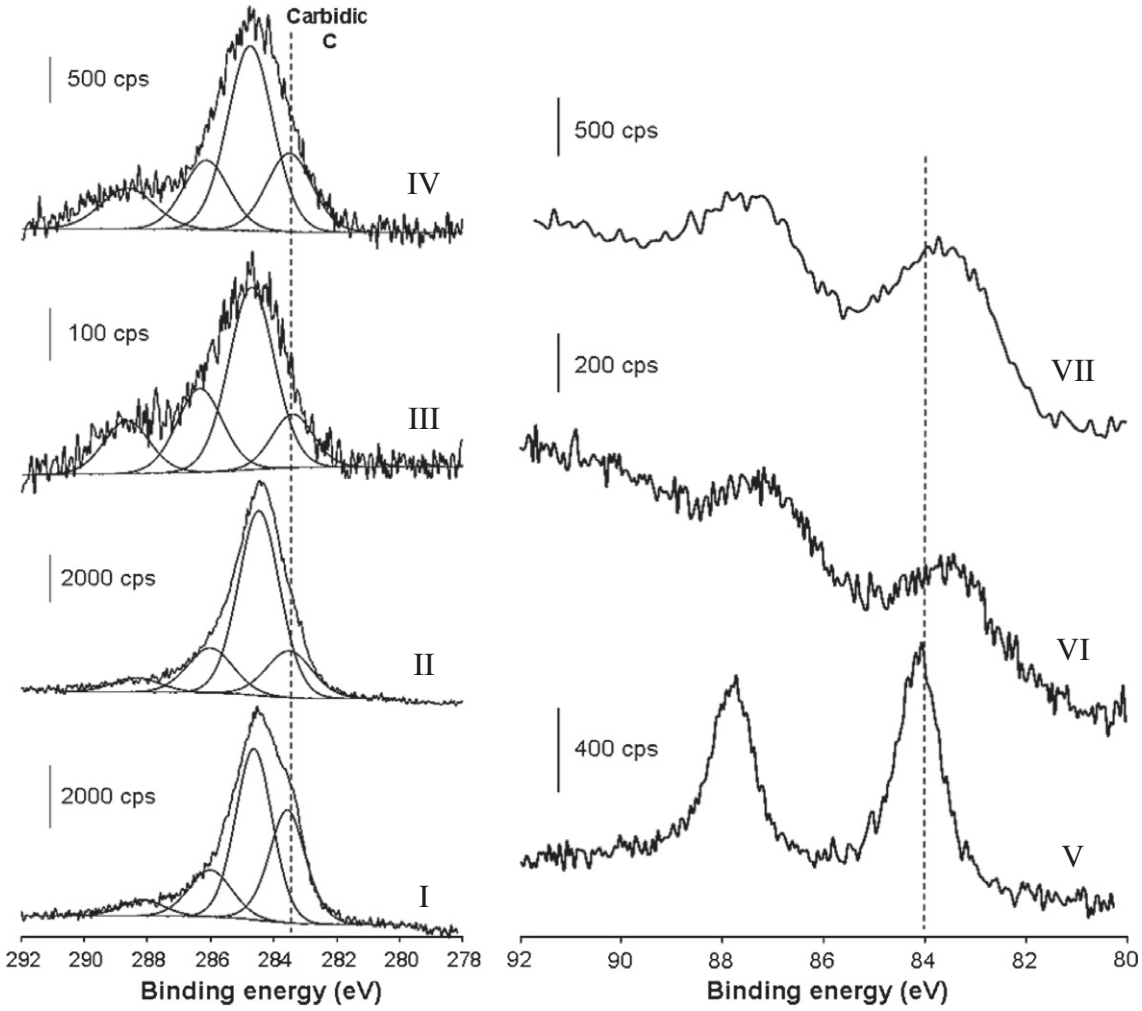

Fig. 7. XPS spectra over the C *1s* region for Mo_2C (I), Au/Mo_2C (II), Mo_2C/Al_2O_3 (III), Au/Mo_2C/Al_2O_3 (IV) and Au 4*f* region for Au/Mo_2C (V), Au/Mo_2C/Al_2O_3 (VI) and Au/Al_2O_3 (VII).

m-DNB (Fig. 8II) involves even greater selectivity demands in terms of partial —NO_2 hydrogenation. We have chosen *m*-DNB as a model reactant because the partially hydrogenated *m*-nitroaniline (*m*-NAN) product is commercially important in the manufacture of polymers and dyes [37]. Earlier work has established that complete reduction to *m*-phenylenediamine (*m*-PDM) is achieved over supported Ni while the *m*-DNB → *m*-NAN step is selectively promoted over supported Au at low levels of conversion [36]. The existing literature on the hydrogenation of nitroarenes has focused on batch liquid systems operated at elevated pressures [66] that have delivered low selectivities to the target amine [67]. A move from batch liquid to gas phase continuous operation serves to lower the associated energy demands while economies of scale favour continuous processes for large throughput. This is the first reported application of Mo carbide (as both catalyst and Au support) in gas phase nitroarene hydrogenation.

3.2.1. Hydrogenation of para-chloronitrobenzene (p-CNB)

The temporal response of *p*-CNB conversion ($x_{p\text{-CNB}}$) over the five catalyst systems is shown in Fig. 9I, where a decline in activity with time on-stream is in evidence. The temporal variation of conversion has been fitted to a first order exponential decay in order to extract a value for the initial conversion (x_0). The applicability of a pseudo-first order kinetic treatment has been established previously [68]

$$\ln(1-x_0)^{-1} = k\left(\frac{n}{F}\right) \tag{7}$$

where n represents either moles of Mo_2C (n_{Mo2C}) or gold (n_{Au}) and the ratio n/F has the physical significance of contact time. The specific rates obtained from the linear relationships shown Fig. 9II are given in Table 2. All the catalysts were 100% selective in terms of *p*-CNB hydrogenation to the target *p*-CAN product with no evidence of hydrodechlorination or ring hydrogenation. The rate constant, normalised with respect to Mo_2C surface area ($k(\mu mol_{p\text{-CNB}}\ m_{Mo_2C^{-2}}\ h^{-1})$, Table 2) generated for Mo_2C/Al_2O_3 was significantly lower than that recorded for Mo_2C, *i.e.,* supporting the carbide on the alumina carrier inhibited hydrogenation. We can link this to the observed (by XPS, see Fig. 6III) lesser carbidic (or rather oxycarbide) character for the alumina supported system. Moreover, the presence of free carbon (Mo/C = 1.5, Table 2) on the surface can block Mo active sites and limit activity [42]. It has been reported elsewhere [69] that strong interaction between the carbide phase and Al_2O_3 support can render the carbide sites less active in the catalytic decomposition of hydrazine. However, Brungs and coworkers [70] have shown that Mo_2C/Al_2O_3 was more stable in methane reforming than bulk Mo_2C where coke deposition was limited on the supported carbide. Indeed, reaction over Mo_2C/Al_2O_3 was characterised by a significantly higher ratio of the conversion achieved after 3 h to the initial value (x_{3h}/x_0) relative to Mo_2C (Table 2). Loss of activity in gas phase hydrogenation of

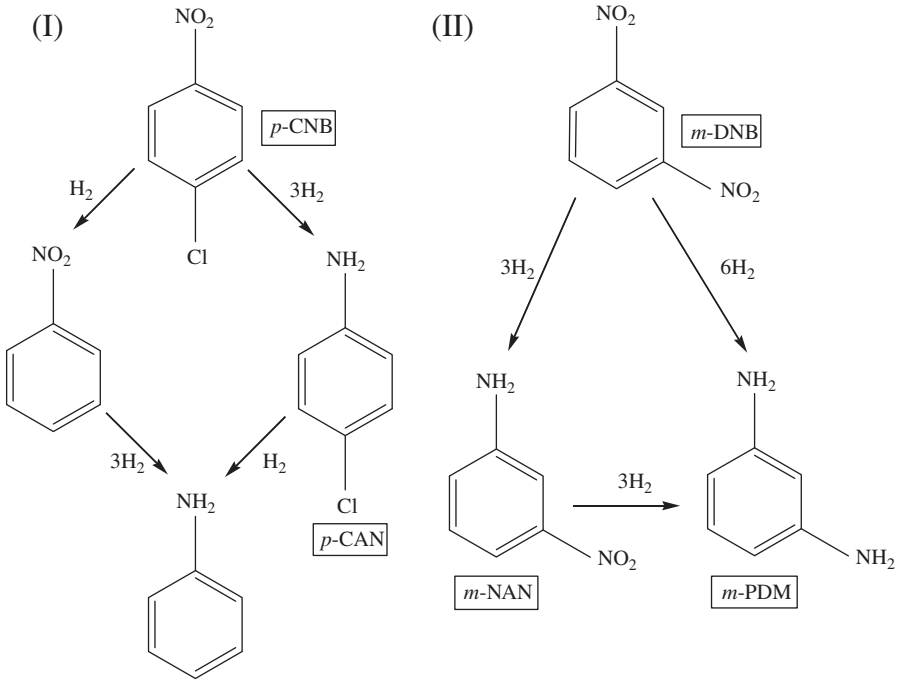

Fig. 8. Reaction pathways in the hydrogenation of *p*-CNB (I) and *m*-DNB (II).

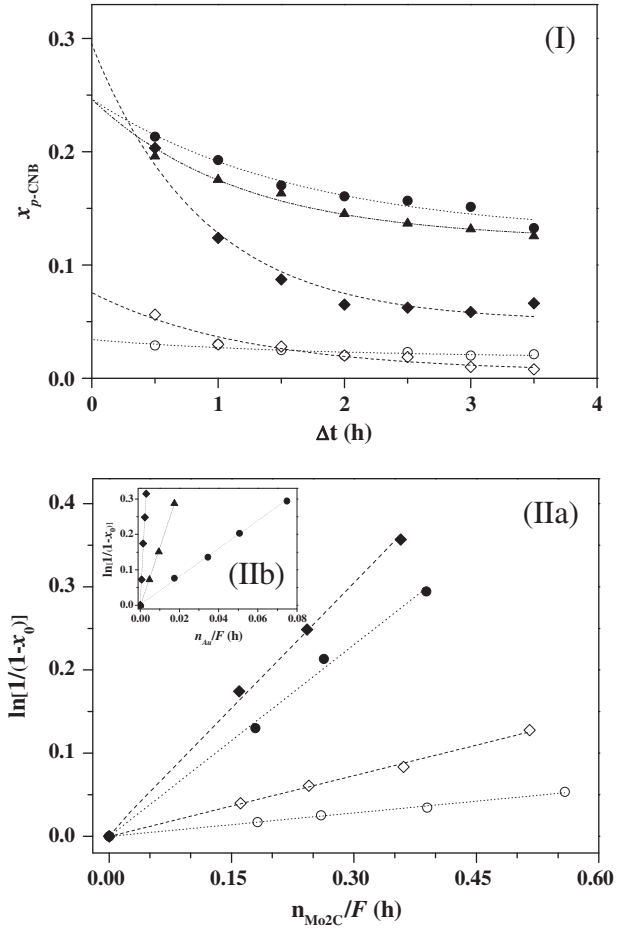

Fig. 9. (I) Variation of *p*-CNB fractional conversion ($x_{p\text{-CNB}}$) with time on-stream. (II) pseudo-first order kinetic plots with respect to (IIa) Mo_2C and (IIb) Au: (◇) Mo_2C, (♦) Au/Mo_2C, (▲) Au/Al_2O_3, (○) Mo_2C/Al_2O_3 and (●) $Au/Mo_2C/Al_2O_3$.

Table 2
Specific rate constant (*k*, with respect to Mo_2C surface area), turnover frequency (*TOF*, with respect to Au dispersion) and ratio of fractional conversion after 3 h to the initial value (x_{3h}/x_0) for the hydrogenation of *p*-CNB.

Catalyst	$k(\mu mol_{p-CNB}\ m_{Mo_2C}{}^{-2}\ h^{-1})$	*TOF* (h^{-1})	$x_{3h}/x_0\ x_0 \approx 0.15$
Mo_2C	36	–	0.12
Mo_2C/Al_2O_3	4	–	0.70
Au/Mo_2C	139	1098	0.12
$Au/Mo_2C/Al_2O_3$	33	27	0.60
Au/Al_2O_3	–	26	0.50

p-CNB has been attributed to metal leaching [71], metal sintering [72], deposition of polymeric products formed by condensation [73], occlusion of active sites by surface carbonate species [74] and poisoning by the water generated during reaction [75]. The introduction of Au (on both Mo_2C and Mo_2C/Al_2O_3) resulted in an appreciable increase in hydrogenation rate, which can be attributed to the catalytic action of both carbide and the supported Au phase. Gold dispersion (Table 1) was obtained from d_{TEM} values [76] and used to determine turnover frequency (*TOF* (h^{-1}), Table 2). We apply *TOF* as a quantitative measure of catalyst performance in terms of the Au component but recognise the contribution of both support (Mo_2C) and metal to the overall hydrogenation rate. Activity in hydrogenation reactions over supported Au has been deemed to be dependent on Au particle size [77]. In previous work [32], we demonstrated an increase (fortyfold) in *p*-CNB hydrogenation rate over oxide supported Au with decreasing particle size (from 9 to 3 nm). As Au/Mo_2C is characterised by a larger mean Au size compared with Au/Al_2O_3, we should expect a lower resultant specific activity. A major finding in this work is the appreciably higher *TOF* delivered by Au/Mo_2C relative to Au/Al_2O_3. We take this as a demonstration of a surface synergism between Au and Mo_2C that results in enhanced catalytic efficiency. Given that the activation of H_2 is rate limiting in hydrogenation reactions over Au, H_2 dissociation on Mo_2C must contribute to the observed elevation of

Table 3
Specific rate constant (k, with respect to Mo_2C surface area), turnover frequency (*TOF*, with respect to Au dispersion) selectivity to *m*-NAN ($S_{m\text{-NAN}}$ at $x_{m\text{-}DNB} \approx 0.05$ and $x_{m\text{-}DNB} \approx 0.15$) and ratio of fractional conversion after 3 h to the initial value (x_{3h}/x_0) for the hydrogenation of *m*-DNB.

Catalyst	$k(\times 10^6)$ ($\mu mol_{m-DNB}\ m_{Mo_2C}^{-2}\ h^{-1}$)	*TOF* (h^{-1})	x_{3h}/x_0	$S_{m\text{-NAN}}$ (%) at $x_{m\text{-}DNB} \approx 0.05$	$S_{m\text{-NAN}}$ (%) at $x_{m\text{-}DNB} \approx 0.15$
Mo_2C	13	–	0.10	100	37
Mo_2C/Al_2O_3	15	–	0.15	100	45
Au/Mo_2C	38	229	0.10	100	56
$Au/Mo_2C/Al_2O_3$	60	50	0.30	85	38
Au/Al_2O_3	–	34	0.10	0[a]	21

[a] 100% selectivity with respect to *m*-PDM.

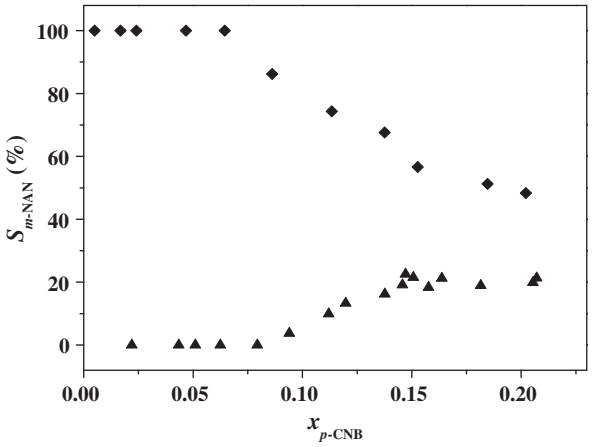

Fig. 10. Variation of *m*-NAN selectivity ($S_{m\text{-NAN}}$) as a function of *m*-DNB fractional conversion ($x_{m\text{-DNB}}$) for reaction over (♦) Au/Mo_2C and (▲) Au/Al_2O_3.

hydrogenation rate, possibly by supplying reactive atomic hydrogen to Au in a "reverse" spillover step.

3.2.2. Hydrogenation of meta-dinitrobenzene (m-DNB)

The hydrogenation of *m*-DNB also exhibited a time on-stream decline that was more severe than observed for *p*-CNB, as can be assessed from the x_{3h}/x_0 entries in Table 3. Alumina supported Mo_2C delivered a comparable specific hydrogenation rate relative to the bulk carbide and retained a higher degree of the initial conversion with time on-stream. Incorporation of Au enhanced hydrogenation performance with an increase in rate (per Mo_2C surface area) by a factor of 3–4. As in the case of *p*-CNB hydrogenation, the *TOF* generated by Au/Mo_2C was significantly greater than that recorded for Au/Al_2O_3. The hydrogenation of *m*-DNB presents a particular challenge in terms of selectivity where *m*-NAN, as the target product, can serve as a reactive intermediate in the formation of *m*-PDM (Fig. 8II). Any meaningful comparison of hydrogenation selectivity is only feasible at a common fractional *m*-DNB conversion ($x_{m\text{-DNB}}$): selectivity values are given in Table 3 where $x_{m\text{-}DNB} \approx 0.05$ and 0.15. The variation of *m*-NAN and *m*-PDM selectivity (S) as a function of $x_{m\text{-}DNB}$ is presented Fig. 10 for reaction over Au/Mo_2C and Au/Al_2O_3. At low fractional conversions ($x_{m\text{-}DNB} < 0.06$), Mo_2C exhibited 100% selectivity to *m*-NAN, with decreasing selectivity at higher conversions; *m*-PDM was the principal product where $x_{m\text{-}DNB} > 0.15$. Au/Mo_2C also exhibited reaction exclusivity in terms of *m*-NAN production at low $x_{m\text{-}DNB}$ (Fig. 10, $x_{m\text{-}DNB} < 0.07$) with a switch to preferential *m*-PDM formation at higher conversions ($x_{m\text{-}DNB} > 0.20$); see also entries in Table 3. The net effect is a significantly higher rate of *m*-NAN production over Au/Mo_2C (0.18 $g_{m\text{-NAN}}\ g_{catalyst}^{-1}\ h^{-1}$, where $x_{m\text{-DNB}} < 0.20$) compared with Mo_2C (0.05 $g_{m\text{-NAN}}\ g_{catalyst}^{-1}\ h^{-1}$, where $x_{m\text{-DNB}} < 0.12$). In complete contrast, Au/Al_2O_3 (Fig. 10) generated *m*-PDM as the principal product ($S > 80\%$), regardless of $x_{m\text{-}DNB}$. The hydrogenation of nitroarenes has been proposed to proceed *via* a nucleophilic mechanism, where a weak nucleophilic agent (hydrogen) attacks the activated —NO_2 group(s) [78]. Differences in reaction selectivity can be associated with differences in the mode of reactant adsorption on the catalyst surface where *m*-NAN formation requires an intermediate resonance structure with a single delocalised positive charge on the ring, *i.e.*, only one —NO_2 group is activated for nucleophilic attack. *m*-PDM results from the formation of a resonance structure with two positive localised charges on the ring where both —NO_2 groups are activated. We have previously attributed differences in *m*-DNB hydrogenation selectivity to the electronic character of the Au sites where adsorption on $Au^{\delta-}$ results in repulsion between the π-delocalised electrons and the partially (negatively) charged gold resulting in the formation of a resonance structure with two positive localised charges on the ring and both —NO_2 groups are activated. The latter effect predominates in the case of Au/Al_2O_3 and is consistent with the XPS response that shows electron transfer from Al_2O_3 to Au. We can associate the selectivity of Au/Mo_2C towards *m*-NAN, in part, to interactions with Au sites that (based on XPS measurements) do not bear a partial negative charge and which favour the formation of a resonance form with a single delocalised positive charge on the ring where only one of the —NO_2 groups is activated [79]. We cannot discount possible *m*-DNB activation *via* interactions with Mo_2C and/or at the Au/carbide interface which, from a consideration of the catalytic response, favour *m*-NAN formation. Our results demonstrate that the use of Mo_2C as support serves to both enhance hydrogenation rate and influence selectivity.

4. Conclusions

We report the first synthesis of gold catalysts supported on molybdenum carbide (Mo_2C and Mo_2C/Al_2O_3); gold was deposited by deposition–precipitation of $HAuCl_4$ (as precursor) with urea. The (β-phase) Mo_2C support was prepared by a temperature programmed carburisation and confirmed by XRD analysis. Mo_2C was characterised by a lower pH_{PZC} (2.9) when compared with Mo_2C/Al_2O_3 (3.7) and Al_2O_3 (7.5). In the synthesis of Au/Mo_2C and $Au/Mo_2C/Al_2O_3$, solution pH exceeded support pH_{PZC} resulting in a less favourable interaction with the anionic Au precursor. The latter effect led to a poorer dispersion of Au relative to Au/Al_2O_3. The formation of metallic Au was observed during Au/Mo_2C preparation and can be attributed to the lower electrochemical potential of the passivated carbide support with a consequent reductive deposition of Au. Preparation of $Au/Mo_2C/Al_2O_3$ was accompanied by a significant Mo leaching into solution, and the supported Mo_2C phase exhibited lesser carbidic character than bulk Mo_2C. This paper is the first reported application of Au/Mo carbide combinations as catalytic materials. Our results for the gas phase hydrogenation of substituted nitroarenes have established a synergism where the combined catalytic action of Au with Mo_2C resulted in higher hydrogenation efficiency for the conversion of *p*-CNB and *m*-DNB, exceeding the performance of Au/

Al_2O_3. In the hydrogenation of *m*-DNB, exclusive formation of the partially reduced *m*-NAN was enhanced over Au/Mo_2C relative to Mo_2C under conditions where Au/Al_2O_3 was non-selective. Further work will focus on synthesis strategies to control Au dispersion with a mechanistic analysis of nitroarene hydrogenation over these catalysts.

Acknowledgments

The authors would like to thank Dr. Christophe Méthivier for performing the XPS analyses and Patricia Beaunier for the HRTEM measurements.

References

[1] A.M. Alexander, J.S.J. Hargreaves, Chem. Soc. Rev. 39 (2010) 4388.
[2] R. Kojima, K. Aika, Appl. Catal. A: Gen. 219 (2001) 141.
[3] P.A. Aegerter, W.W.C. Quigley, G.J. Simpson, D.D. Ziegler, J.W. Logan, K.R. McCrea, S. Glazier, M.E. Bussell, J. Catal. 164 (1996) 109.
[4] A. Szymańska-Kolasa, M. Lewandowski, C. Sayag, G. Djéga-Mariadassou, Catal. Today 119 (2007) 7.
[5] P.M. Patterson, T.K. Das, B.H. Davis, Appl. Catal. A: Gen. 251 (2003) 449.
[6] N.M. Schweitzer, J.A. Schaidle, O.K. Ezekoye, X. Pan, S. Linic, L.T. Thompson, J. Am. Chem. Soc. 133 (2011) 2378.
[7] A.C. Lausche, J.A. Schaidle, L.T. Thompson, Appl. Catal. A: Gen. 401 (2011) 29.
[8] J.S. Lee, S. Locatelli, T. Oyama, M. Boudart, J. Catal. 125 (1990) 157.
[9] S.T. Oyama, Catal. Today 15 (1992) 179.
[10] H. Liu, J. Zhu, Z. Lai, R. Zhao, D. He, Scr. Mater. 60 (2009) 949.
[11] J.G. Chen, Chem. Rev. 96 (1996) 1477.
[12] E.K. Storms, The Refractory Carbides, Academic Press, New York and London, 1967.
[13] K.Y. Park, W.K. Seo, J.S. Lee, Catal. Lett. 11 (1991) 349.
[14] J.-G. Choi, J.R. Brenner, L.T. Thompson, J. Catal. 154 (1995) 33.
[15] L. Volpe, M. Boudart, J. Solid State Chem. 59 (1985) 332.
[16] K.T. Jung, W.B. Kim, C.H. Rhee, J.S. Lee, Chem. Mater. 16 (2004) 307.
[17] X.-H. Wang, H.-L. Hao, M.-H. Zhang, W. Li, K.-Y. Tao, J. Solid State Chem. 179 (2006) 538.
[18] G. Ertl, H. Knözinger, J. Weitkamp, Preparation of Solid Catalysts, Wiley-VCH, Weinheim, 1999.
[19] D.J. Sajkowski, S.T. Oyama, Appl. Catal. A: Gen. 134 (1996) 339.
[20] J.S. Lee, M.H. Yeom, K.Y. Park, I.-S. Nam, J.S. Chung, Y.G. Kim, S.H. Moon, J. Catal. 128 (1991) 126.
[21] S.J. Ardakani, X. Liu, K.J. Smith, Appl. Catal. A: Gen. 324 (2007) 9.
[22] Q.L. Zhu, B. Zhang, J. Yang, J.X. Wang, J. Zhao, S.F. Ji, H.Q. Wang, New J. Chem. 27 (2003) 1633.
[23] M. Lewandowski, A. Szymańska-Kolasa, P.D. Costa, C. Sayag, Catal. Today 119 (2007) 31.
[24] Espinoza-Monjardín, J. Cruz-Reyes, M.D. Valle-Granados, E. Flores-Aquino, M. Avalos-Borja, S. Fuentes-Moyado, Catal. Lett. 120 (2008) 137.
[25] M.-L. Frauwallner, F. López-Linares, J. Lara-Romero, C.E. Scott, V. Ali, E. Hernández, P. Pereira-Almao, Appl. Catal. A: Gen. 394 (2011) 62.
[26] B. Hammer, J.K. Norskov, Nature 376 (1995) 238.
[27] A. Corma, P. Serna, Science 313 (2006) 332.
[28] C. Milone, R. Ingoglia, A. Pistone, G. Neri, F. Frusteri, S. Galvagno, J. Catal. 222 (2004) 348.
[29] J.E. Bailie, G.J. Hutchings, J.C.S. Chem. Commun. (1999) 2151.
[30] A. Hugon, L. Delannoy, C. Louis, Gold Bull. 41 (2008) 127.
[31] S.A. Nikolaev, V.V. Smirnov, Gold Bull. 42 (2009) 182.
[32] F. Cárdenas-Lizana, S. Gómez-Quero, N. Perret, M.A. Keane, Gold Bull. 42 (2009) 124.
[33] E. Florez, F. Viñes, J.A. Rodriguez, F. Illas, J. Chem. Phys. 130 (2009) 244706.
[34] F. Cárdenas-Lizana, S. Gómez-Quero, M.A. Keane, Catal. Commun. 9 (2008) 475.
[35] F. Cárdenas-Lizana, S. Gómez-Quero, M.A. Keane, ChemSusChem 1 (2008) 215.
[36] F. Cárdenas-Lizana, S. Gómez-Quero, N. Perret, M.A. Keane, Catal. Sci. Technol. 1 (2011) 652.
[37] V.L. Khilnani, S.B. Chandalia, Org. Proc. Res. Dev. 5 (2001) 263.
[38] J. Xiong, J.X. Chen, J.Y. Zhang, Catal. Commun. 8 (2007) 345.
[39] Y.S. Kwon, A.A. Gromov, A.P. Ilyin, A.A. Ditts, J.S. Kim, S.H. Park, M.H. Hong, Int. J. Refract. Met. Hard Mater. 22 (2004) 235.
[40] A. Hugon, N. El Kolli, C. Louis, J. Catal. 274 (2010) 239.
[41] J. Vakros, C. Kordulis, A. Lycourghiotis, Chem. Commun. 17 (2002) 1980.
[42] J.S. Choi, G. Bugli, G. Djéga-Mariadassou, J. Catal. 193 (2000) 238.
[43] M.A. Keane, J. Mol. Catal. A: Chem. 118 (1997) 261.
[44] F. Moreau, G.C. Bond, Catal. Today 122 (2007) 215.
[45] R. Zanella, C. Louis, Catal. Today 107 (2005) 768.
[46] S. Gomez-Quero, F. Cardenas-Lizana, M.A. Keane, Ind. Eng. Chem. Res. 47 (2008) 6841.
[47] F. Moreau, G.C. Bond, A.O. Taylor, J. Catal. 231 (2005) 105.
[48] B.A.A. Silberova, G. Mul, M. Makkee, J.A. Moulijn, J. Catal. 243 (2006) 171.
[49] N.A. Hodge, C.J. Kiely, R. Whyman, M.R.H. Siddiqui, G.J. Hutchings, Q.A. Pankhurst, F.E. Wagner, R.R. Rajaram, S.E. Golunski, Catal. Today 72 (2002) 133.
[50] N.N. Greenwood, A. Earnshaw, Chemistry of the Elements, second ed., Butterworth-Heinemann, Oxford, UK, 1997.
[51] I. Dobrosz, K. Jiratova, V. Pitchon, J.M. Rynkowski, J. Mol. Catal. A: Chem. 234 (2005) 187.
[52] H.S. Oh, J.H. Yang, C.K. Costello, Y.M. Wang, S.R. Bare, H.H. Kung, M.C. Kung, J. Catal. 210 (2002) 375.
[53] M. Trueba, S.P. Trasatti, Eur. J. Inorg. Chem. 17 (2005) 3393.
[54] A.C. Gluhoi, X. Tang, P. Marginean, B.E. Nieuwenhuys, Top. Catal. 39 (2006) 101.
[55] A. Saadi, Z. Rassoul, M.M. Bettahar, J. Mol. Catal. A: Chem. 164 (2000) 205.
[56] J.R. Regalbuto, J.-W. Ha, Catal. Lett. 29 (1994) 189.
[57] A.R.S. Darujati, W.J. Thomson, Appl. Catal. A: Gen. 296 (2005) 139.
[58] B. Diaz, S.J. Sawhill, D.H. Bale, R. Main, D.C. Phillips, S. Korlann, R. Self, M.E. Bussell, Catal. Today 86 (2003) 191.
[59] M. Shimoda, T. Hirata, K. Yagisawa, M. Okochi, A. Yoshikawa, J. Mater. Sci. Lett. 8 (1989) 1089.
[60] Z.B.Z. Wei, P. Grange, B. Delmon, Appl. Surf. Sci. 135 (1998) 107.
[61] T.P. St Clair, S.T. Oyama, D.F. Cox, S. Otani, Y. Ishizawa, R.L. Lo, K. Fukui, Y. Iwasawa, Surf. Sci. 426 (1999) 187.
[62] S.D. Gardner, C.S.K. Singamsetty, G.L. Booth, G.R. He, C.U. Pittman, Carbon 33 (1995) 587.
[63] W.C. Wu, Z.L. Wu, C.H. Liang, P.L. Ying, Z.C. Feng, C. Li, Phys. Chem. Chem. Phys. 6 (2004) 5603.
[64] A.V. Naumkin, A.Y. Vasil'kov, I.O. Volkov, V.V. Smirnov, S.A. Nikolaev, Inorg. Mater. 43 (2007) 381.
[65] Y.F. Han, Z.Y. Zhong, K. Ramesh, F.X. Chen, L.W. Chen, T. White, Q.L. Tay, S.N. Yaakub, Z. Wang, J. Phys. Chem. C 111 (2007) 8410.
[66] A. Corma, P. Serna, Nat. Protoc. 1 (2006) 2590.
[67] K. Koprivova, L. Červený, Res. Chem. Intermed. 34 (2008) 93.
[68] F. Cárdenas-Lizana, S. Gómez-Quero, M.A. Keane, Appl. Catal. A: Gen. 334 (2008) 199.
[69] J. Sun, M. Zheng, X. Wang, A. Wang, R. Cheng, T. Li, T. Zhang, Catal. Lett. 123 (2008) 150.
[70] A.J. Brungs, A.P.E. York, J.B. Claridge, C. Márquez-Alvarez, M.L.H. Green, Catal. Lett. 70 (2000) 117.
[71] Y.Y. Chen, C.A. Wang, H.Y. Liu, J.S. Qiu, X.H. Bao, Chem. Commun. (2005) 5298.
[72] J. Chen, N. Yao, R. Wang, J. Zhang, Chem. Eng. J. 148 (2009) 164.
[73] V. Kratky, M. Kralik, M. Mecarova, M. Stolcova, L. Zalibera, M. Hronec, J. Mol. Catal. A: Chem. 235 (2002) 225.
[74] Y. Hao, R. Liu, X. Meng, H. Cheng, F. Zhao, J. Mol. Catal. A: Chem. 335 (2011) 183.
[75] P. Sangeetha, P. Seetharamulu, K. Shanthi, S. Narayanan, K.S.R. Rao, J. Mol. Catal. A: Chem. 273 (2007) 244.
[76] J.J.F. Scholten, A.P. Pijpers, A.M.L. Hustings, Catal. Rev. – Sci. Eng. 27 (1985) 151.
[77] A. Corma, P. Serna, P. Concepcion, J.J. Calvino, J. Am. Chem. Soc. 130 (2008) 8748.
[78] F. Cárdenas-Lizana, Z.M.D. Pedro, S. Gómez-Quero, M.A. Keane, J. Mol. Catal. A: Chem. 326 (2010) 48.
[79] F. Cárdenas-Lizana, S. Gómez-Quero, N. Perret, L. Kiwi-Minsker, M.A. Keane, Catal. Sci. Technol. 1 (2011) 794.